Study of fluid-structure-contact interactions for ink transfer modelling in a contact-based printing system

Mehdi Seddiq, Phillip Taylor, Leon Newton, Martin Sharp, Mehdi Seddighi

Journal of Computational Design and Engineering, 2026, **13**, 45–59
DOI: 10.1093/jcde/qwaf119
Advance access publication date: 4 November 2025
Research Article

Study of fluid-structure-contact interactions for ink transfer modelling in a contact-based printing system

Mehdi Seddiq, Phillip Taylor, Leon Newton, Martin Sharp and Mehdi Seddighi*

School of Engineering, Liverpool John Moores University, Liverpool L3 3AF, UK
*Correspondence: m.seddighi@ljmu.ac.uk

Abstract

Fluid–structure–contact interaction (FSCI) phenomena have been studied in recent years for only a limited range of applications, such as the interaction of air with multiple parachute canopies and blood flow through heart valves. Ink transfer in contact-based printing systems, such as flexographic printers, is a significant example of such phenomena and can be adequately understood only when investigated as an FSCI problem. This paper aims to pioneer the study of ink transfer between interacting rollers by proposing a methodology applicable to a wide range of FSCI scenarios. The methodology includes prescribing a small gap where the structures establish physical contact and applying an auxiliary fluid in the gap with a viscosity high enough to prohibit its movement, thereby practically replicating the real closed contact. A Lagrangian conformal mesh approach is employed to maximise accuracy while maintaining reasonable computational cost. Simulations were conducted on a scenario involving substantial deformation of a roller surface and its penetration into the microcavities of the other roller, where the ink initially resides. The results demonstrate different phases of ink transfer between surfaces: pre-contact, contact development, isolation, contact opening, and surface separation, during which ink breakup occurs. The pressure was observed to rise significantly during the penetration phase, reaching a peak value of approximately 1×10^6 Pa. The ink transfer rate was calculated to be 27%, consistent with the relatively lower band of reported industrial ranges. The ink transfer rate was calculated to be 27%, consistent with the relatively lower band of reported industrial ranges. These findings provide insights into understanding and controlling ink transfer between rollers, which can help maximise cell evacuation rates by altering the engraved texture shapes on the rollers. The proposed methodology is also applicable to other contact-based printing systems and broader applications involving FSCIs.

Keywords: fluid-structure-contact interactions, fluid-structure interaction, computational fluid dynamics, structural analysis, contact-based printing

1. Introduction

Fluid-structure-contact interactions (FSCIs) phenomena involve dynamic contact between two structures, forming part of a fluid boundary. This process includes the physical connection or separation of two surfaces within the fluid domain, with the fluid occupying the space between the structures as the contact opens. Modelling such processes presents unique challenges not encountered in traditional fluid-structure interaction (FSI) or other fluid flow problems. Structural contact plays a critical role in contact-based printing presses, such as flexographic printers, where a series of high-speed rollers work to transfer ink from the initial ‘bath’ to the substrate. Each point of transfer between a pair of rollers represents an individual FSCI problem, where the effective width of the fluid domain shrinks to zero. The necessary precision of the printing medium requires precise control of the delivered ink volume and its distribution. Hence, accurate modelling of these interactions is critical for optimizing ink transfer rates at each stage.

In printing, the ink volume is controlled by a metal roller, with small grooves embedded in its surface (Kipphan, 2001). A ‘doctor blade’ removes the thick layer of ink from the surface, such that only the ink within the grooves remains. In flexographic printing, the anilox roller—an engraved metering roller controlling ink delivery—features a dense, uniform array of grooves. A subsequent roller consists of a metal core, covered with an elastic plate, on which the printing pattern is imprinted through protrusions. In gravure printing, the grooves on the roller (gravure roller) are themselves arranged in the printing pattern. Thus, ink can be transferred to the substrate either directly from the gravure roller or from a smooth, elastic roller acting as an intermediary (gravure offset printing). In these cases, roller-to-roller contact comprises four general stages: (i) initial approach of the surface, (ii) surface-to-surface contact and initial ink contact, (iii) surface-to-surface separation and ink deformation, and finally (iv) separation of the ink volume. Stages (ii) and (iii) are the most challenging to study numerically, not only due to the temporary vanishing of fluid volumes but also due to the increasingly infinitesimal gap size that appears shortly before contact.

Experimental and numerical studies have explored the full cycle of stages for the simplified case of a single ink droplet and two flat plates (Ahmed *et al.*, 2011; Park *et al.*, 2012). Primarily, these studies identified that the ink transfer rate is dependent on both the velocity of separation and the contact angle of each surface. Meanwhile, numerical investigations within ink cells have focused overwhelmingly on the separation stage, in part due to the complexity of modelling FSCI interactions during the preceding stages. The studies of Huang *et al.* (2008) and Ghadiri *et al.*

Received: April 27, 2025. **Revised:** September 22, 2025. **Accepted:** September 23, 2025

(2011) investigated the influence of cell geometry on transfer rate during separation in gravure offset printing. A similar study by Dong *et al.* (2021) investigated the influence of cell geometry on ink pick-up rate in the application of standard Gravure printing. When considering only the separation stage, the ink volume was modelled as being in contact with the upper surface, with a distribution that was estimated from preliminary steady-state models (Huang *et al.*, 2008; Ghadiri *et al.*, 2011; Wu *et al.*, 2019; Dong *et al.*, 2021). In addition to its uncertainty, this approach must further assume that cell geometry has a negligible impact on the behaviour of ink flow prior to separation. This approach assumes the ink body reaches equilibrium, irrespective of post–separation conditions. An experimental analysis using a horizontally moving curved glass plate found that ink transfer was significantly lower when a gap remained between the elastic surface and the cell crests (Yin & Kumar, 2006). It further identified that the presence of deformation/penetration had a negligible effect on the transfer rate during contact. However, the analysis was limited to low values of deformation for the elastic surface. The latter observation suggests that for standard gravure printing, a rigid surface assumption may be acceptable given the low elasticity of the substrate. However, the former observation suggests that excluding the effects of direct surface-to-surface contact underestimates the overall ink transfer rate.

Beyond structural contact, advanced numerical techniques such as arbitrary Lagrangian–Eulerian (ALE), immersed boundary methods, and mesh-free approaches like smoothed particle hydrodynamics have been effectively applied to model complex FSI phenomena. Applications range from modelling cardiovascular biomechanics and heart valve dynamics to aquatic locomotion and bio-inspired robotic systems. These advancements address challenges in simulating large deformations, dynamically changing interfaces, and multi-domain energy coupling (Pramanik *et al.*, 2024).

To the best of the authors' knowledge, numerical investigations of true FSCI applications are currently limited to a small number of specialized applications, such as the expansion and contact between multiple parachute canopies during descent (Takizawa & Tezduyar, 2012; Cao *et al.*, 2017), and pulsating blood flow through biological valves in cardiovascular systems (Griffith *et al.*, 2009; Hsu *et al.*, 2014; Spuhler *et al.*, 2018; Sun *et al.*, 2021). There are at least two aspects of FSCI that are distinct from other fluid flow processes in numerical modelling. First, it is necessary to model interactions between the structures, which entails a study beyond the context of fluid mechanics. The second aspect is the presence of a gap with extremely small or almost zero width between moving walls in the fluid domain. In respect of numerical modelling, there is no space between overlapping surfaces to place fluid elements. Indeed, it is problematic even to preserve mesh quality in locations with small gaps, which is a primary challenge in the numerical modelling of FSCI problems.

Gap handling. In modelling surface-to-surface contact in FSI, there are two primary considerations. The first is detecting imminent contact points and avoiding surface penetration. The simplest method for handling this is to limit freedom of movement immediately prior to contact. For example, in the case of rigid, biomechanical heart valves, direct contact detection can be avoided by restricting the angle of rotation to a pre-defined window of motion (Borazjani *et al.*, 2008, 2013; Banks *et al.*, 2018). Near the rotation limit, the model applies a repulsive torque and a damping term that reduce angular acceleration.

In contrast, for free-moving elastic leaflets undergoing large deformations, the point of contact cannot be predicted. For mirrored pairs of elastic structures, this limit can be imposed as a slip condition on an asymmetric boundary condition, provided the zone of contact lies parallel to the boundary, and the structures are ideally mirrored. When the plane of contact is unknown, continuous modelling of discrete point-to-point contact for multiple leaflets (Borazjani, 2013; Chen & Luo, 2018) must be applied to prevent penetration of the arbitrarily deforming surfaces. The second consideration lies in modelling the blockage effects due to contact. Many studies have opted to ignore the effects of leakage, assuming that the specified threshold is sufficiently small to restrict leakage to negligible values during contact (Calandrini & Aulisa, 2019; Joda *et al.*, 2019; Sun *et al.*, 2021). However, to further minimize leakage, the hydraulic resistance within the remaining gap can be artificially amplified to reduce the flow rate (Bavo *et al.*, 2016). Ager et al. (2019) incorporated the effects of macroscale surface roughness into their contact model by representing the macrostructure as a homogeneous poro-elastic layer applied over the surface of one of the solid boundaries. As the poro-elastic layer compresses due to contact with the opposing surface, the fluid–solid fraction decreases, hindering fluid motion through the layer. In monolithic solvers, fluid cells spanning the contact zone can be converted into solid cells until separation is detected (Spuhler *et al.*, 2018). While this approach eliminates leakage, monolithic solvers are far less standard than coupled fluid–solid domains, which limits the range of available tools and packages.

Immersed boundary methods. Immersed boundary methods represent the fluid–solid interface as an arbitrary boundary which is imposed on the fluid domain. A critical advantage of immersed methods is their ability to handle large displacements and contact between structures without distorting the underlying mesh. Although initially developed for modelling thin elastic leaflets in heart valves (Peskin, 1977), further advancements produced immersed methods that handle rigid immersed boundaries (Fadlun *et al.*, 2000; Rajat Mittal & Iaccarino, 2005) and improve the resolution of sharp interfaces (Ge & Sotiropoulos, 2007; R. Mittal *et al.*, 2008). The accuracy of immersed boundaries relies heavily on the suitability of the forcing terms and the interpolation method to project the cells onto the wall. Furthermore, they can be combined with conformal mesh techniques (Astorino *et al.*, 2009; De Hart *et al.*, 2003; Hsu *et al.*, 2014) to simultaneously model the deformations of thin elastic structures and larger scale deformations, such as those experienced by the arterial walls. Gerosa (2021) developed an unfitted mesh contact scheme in which cells can be dynamically split when multiple immersed boundaries occupy the same cell. In this way, the domain can efficiently maintain a single layer of fluid cells between intersecting or overlapping surfaces.

Conformal mesh methods. In conformal mesh methods, the mesh of the fluid domain is aligned with the geometry of the fluid–solid interface. The mesh in the fluid domain is permitted to deform in order to maintain this alignment with the moving fluid–solid interface. The ALE method, introduced by Donea *et al.* (1982), is one of the most common approaches for modelling FSI in conformal meshes. The solid domain has a fully Lagrangian representation, whilst the velocity of the mesh displacement in the fluid domain is included in the convective terms of the conservation equations to combine the Eulerian representation of the fluid with the Lagrangian representation of the mesh into a single domain. When the fluid–solid boundary undergoes a large displacement, distortion of the fluid mesh can cause severe degradation of mesh quality. This issue is common in the modelling of FSCI applications, where, as the distance between two surfaces approaches zero, the fluid cells in the gap undergo exponential compression. For this reason, simulations may employ algorithms to re-mesh the domain once an excessive degradation in cell quality has been detected (Souli *et al.*, 2000). Alternatively, the fluid–solid boundary may be permitted to move between cell edges once an excessive degradation in cell quality is detected (Basting *et al.*, 2017). For a simpler geometry of a rigid biomechanical valve, stable simulations using the ALE method have been successfully validated when applied with frequent re-meshing during contact (Nobili *et al.*, 2008). The conformal mesh methods are capable of accurately representing the boundary because they do not rely on additional forcing terms or interpolation from cell centres to the fluid-structure contact line. However, the requirements for re-meshing, which are inefficient in parallel processing, can significantly impact overall efficiency. The study by Bavo *et al.* (2016) performed a direct comparison between the ALE and immersed boundary methods for modelling contact between elastic leaflets in a prosthetic aortic valve. The initial cell count in the immersed boundary methods was greater than in the conformal mesh case by a factor of four, in order to avoid the continuous mesh refinement which would be required to maintain near-wall resolution (Griffith *et al.*, 2009).

Nevertheless, the conformal mesh case took significantly longer due to the high frequency of mesh generation required. Subsequent studies into cardiovascular valves have shown that simulations are viable, even without re-meshing, if the model is simplified to a 2D domain (Calandrini & Aulisa, 2019; Joda *et al.*, 2019). The investigations of Spühler *et al.* (2018) modelled FSCI interaction between fully 3D elastic leaflets. Despite large deformation and gap shrinkage, they were able to maintain sufficient mesh quality purely through optimized smoothing algorithms alone. However, to maintain stability during approach and contact, the time-step interval had to be reduced by a factor of 50. Hence, the avoidance of serialized meshing algorithms was counteracted by a significant increase in solver iterations.

While this study focuses on ink transfer in contact-based printing systems, it is worth noting that other printing and microfluidic technologies, such as microcontact printing and dip-pen nanolithography, are also contact-based and involve ink transfer (Mondal & McMurtrey 2020). For example, microcontact printing uses an elastomeric stamp to transfer patterns of ink or molecules onto a substrate through physical contact, and dip-pen nanolithography relies on nanoscale ink deposition via an atomic force microscope tip. In addition, traditional printing methods such as gravure, offset, and inkjet printing (Kipphan, 2001) provide important context for understanding the unique contributions of flexographic printing. Gravure printing shares similarities with flexography by using engraved rollers to transfer ink, but the ink transfer is governed by the geometry of recessed cells and the interaction with a doctor blade. Offset printing, in contrast, uses an intermediary blanket roller to transfer ink indirectly from a plate to the substrate, ensuring high-quality prints with minimal substrate contact. Inkjet printing represents a non-contact approach, where ink is ejected in precise droplets via thermal, piezoelectric, or continuous mechanisms. Unlike these methods, flexographic and gravure printing rely heavily on mechanical pressure and deformation during roller-to-roller contact, phenomena that are central to the FSCIs studied in this paper.

The primary contributions of this paper are (i) the design of a model for FSCI processes, and (ii) new insights into ink transfer in a flexographic printer, which serves as an exemplary case of FSCI problems. The modelling contribution is particularly relevant to processes where there is substantial boundary movement, predictable points of contact, fully closed contact, and locked fluid with no leakage tolerated. Examples of such processes include the dynamics of a tyre on a wet surface and gasketed flange connections.

For cases where fluid-domain boundaries experience significant changes due to structural relative motions or substantial deformations, the use of immersed boundary methods is challenging. This challenge arises because the fluid mesh is fixed and does not adapt to accommodate boundary variations, leading to inaccurate representations of FSIs unless a minimal mesh is employed, which incurs substantial computational costs. To meet the requirements of these processes, a method is devised to accommodate gap handling with a conformal mesh.

The second contribution of this paper is the investigation of ink transfer between contacting surfaces, which involves complex processes such as ink breakup. This phenomenon remains inadequately understood in the existing literature, as it suffers from a lack of comprehensive studies addressing the mechanisms of ink transfer (Abbott, 2018). The coupled fluid-structure model proposed in this paper is applied to simulate ink transfer between rollers in a contact-based printing system, thereby enhancing our understanding of the process.

2. Problem Definition

Liquid pick-up is modelled from the cavities (cells) of a rotating roller called the ‘textured-surface’ roller, also referred to as the rigid body, to the surface of another rotating roller called the ‘elastic-surface’ roller, also referred to as the elastic body, which is covered with an elastic polymer sheet. In flexographic printers, these rollers are called the ‘anilox’ and ‘flexo plate’ rollers. Figure 1 shows a schematic of the domain used in the fluid model. A minimized domain size is used to reduce the required computational time. Although the textured roller contains many cavities, the domain includes only a single cavity from the rigid roller and a limited section of the elastic surface, sized adequately to cover the cavity with a small margin around it fully. The rollers are pressed toward each other, causing the elastic material to penetrate the cavities and take on a portion of the liquid. The amount of compression between the rollers is described by the ‘interference’ between the rollers, also known as ‘engagement’, which is defined as the difference between the sum of the rollers’ radii and the distance between their centres. When the interference is zero, the rollers merely touch each other, and no penetration occurs. In addition to the walls representing the rigid and elastic surfaces of the rollers, additional boundaries consisting of walls and a pressure outlet boundary are defined around the bodies to delimit the domain. The pressure outlet boundary aims to connect the domain to a physical pressure.

3. Numerical Procedure

The numerical framework contains a structural analysis, a fluid model, and a fluid-structural coupling scheme, which are described in the following sections.

3.1 Structural analysis model

Structural analysis is used to calculate deformations in the elastic material as it penetrates the cavities on the rigid roller. A model has been developed in ANSYS-Mechanical 2021 with Transient Structural to estimate both the magnitude and curvature of penetration while the contact between the roller surfaces progresses.

The structural model includes sectors of each roller. The surface of the textured-surface roller, i.e., the walls of the cavity, is

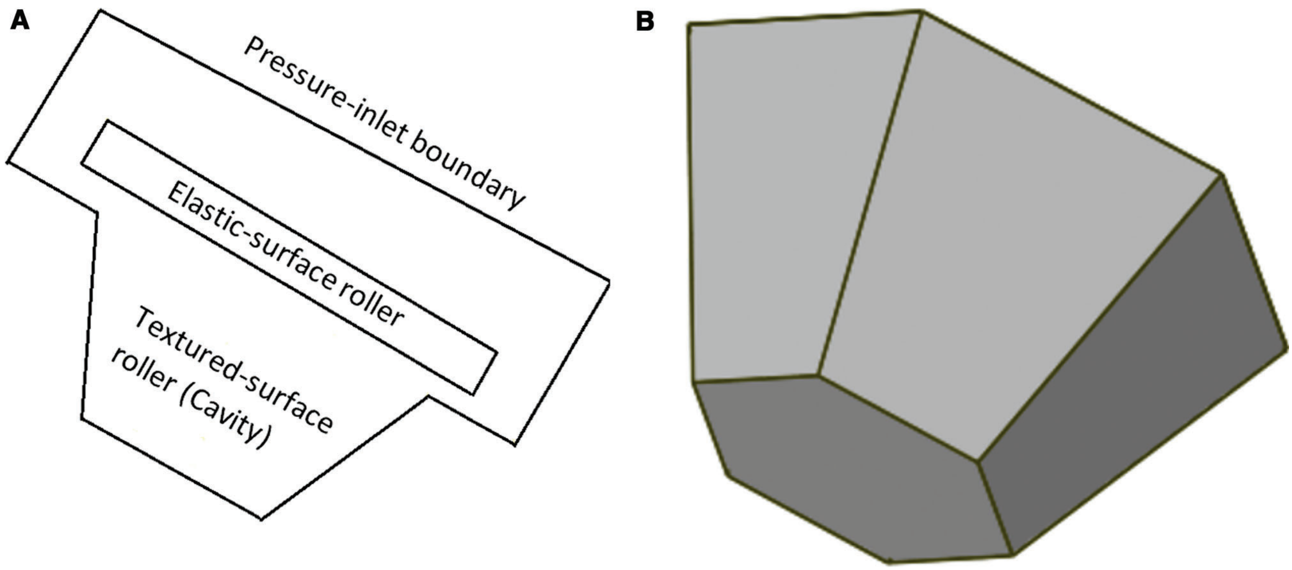

Figure 1: A schematic of the simulation domain, (A) cross-section of the domain, and (B) 3D view of the cavity on the textured roller.

made from a hard material and is considered a rigid body. The other body consists of a flexible material attached to a rigid core in the centre of the elastic roller. The flexible material is made from a rubber-like polymer with a Poisson's ratio of circa 0.5, allowing it to display substantial penetration in small cavities. A linear approximation is assumed for the stress–strain relationship. The governing equation has the following form:

$$M\ddot{u} + C\dot{u} + F^{i} = F^{a} \tag{1}$$

where $\ddot{u} = \ddot{u}(t)$ and $\dot{u} = \dot{u}(t)$ are the acceleration and velocity vectors, M and C are the structural mass and damping matrices, and $F^{i} = F^{i}(t)$ and $F^{a} = F^{a}(t)$ represent the internal and applied load vectors. The stress $\overline{\overline{\sigma}}$ and strain $\overline{\overline{\epsilon}}$ tensors are related by

$$\overline{\overline{\sigma}}a = D\overline{\overline{\epsilon}} \tag{2}$$

where D is the elastic stiffness matrix for the deforming material. More details can be found in ANSYS-Mechanical 2021 R1, Theory Reference.

The contact between the textured- and the elastic-surface roller is modelled as a Bond-type contact. In contrast, the interaction between the cavity walls and the elastic roller surface is treated as frictional contact with a friction coefficient, allowing for small sliding during penetration. In both contacts, an augmented Lagrange method for formulation, and the nodal-normal-from-contact method for detecting contact are used for reasonably accurate modelling of interactions between the surfaces.

3.2 Fluid-structure coupling

The linkage between fluid and structure domains can be modelled using either a monolithic or a partitioned approach. Monolithic models feature strong coupling with frequent data exchange between domains, while partitioned models use looser coupling. While monolithic models offer higher accuracy, partitioned models are computationally less expensive due to reduced coupling requirements. However, comparative studies show that partitioned models may require more iterations and are less accurate, particularly for large deflections (Ha *et al.*, 2017). The stability and accuracy of loose coupling in partitioned models are dependent on the application (Benra *et al.*, 2011).

In an ideal strong coupling scenario, the structural and fluid models operate concurrently, with updated surface profiles passed between models after specific time-steps. However, strong coupling presents challenges, particularly in applications with significant surface contact, where maintaining the desired gaps for the fluid model becomes difficult, and computational costs rise prohibitively. To address these issues, the present study adopts a partitioned model with loose coupling, which establishes an indirect linkage between the fluid and structural models.

The implementation of the loose fluid-structure coupling involves two structural models, and the results of these models are superimposed. The primary structural model considers the interaction between the rollers during rotation, simulating the deformation of the elastic material caused by contact with the rigid roller. From this simulation, the surface profile at each instance of the rollers' interaction is determined, and an initial value for the maximum penetration is obtained. However, the penetration predicted by this model is excessive and does not account for the presence of fluid in the isolated space. The second structural model simulates radial compression, where the elastic material is compressed into the cavity of the rigid roller, directed toward its centre, based on the level of interference. This simulation is conducted twice: first without any additional loading and then with a constant pressure applied within the cavity. Based on the resulting reduction in the penetration of the elastic material, the profile obtained from the main simulation is adjusted. This modified profile is then applied in the fluid model, and the updated fluid pressure is assessed to determine whether further iterations are required. The deformation of the polymer in the radial model was found to be proportional to the pressure, and as such, the deformations are updated through manual calculations. A schematic showing the fluid-structural coupling feedback workflow is illustrated in Figure 2.

3.3 Fluid model

Figure 1 shows the geometry used in the simulations. Given that a loose coupling is adopted between the structure and fluid models, after completing the structural analysis, the profile of the elastic surface at various stages is determined, and all fluid-domain

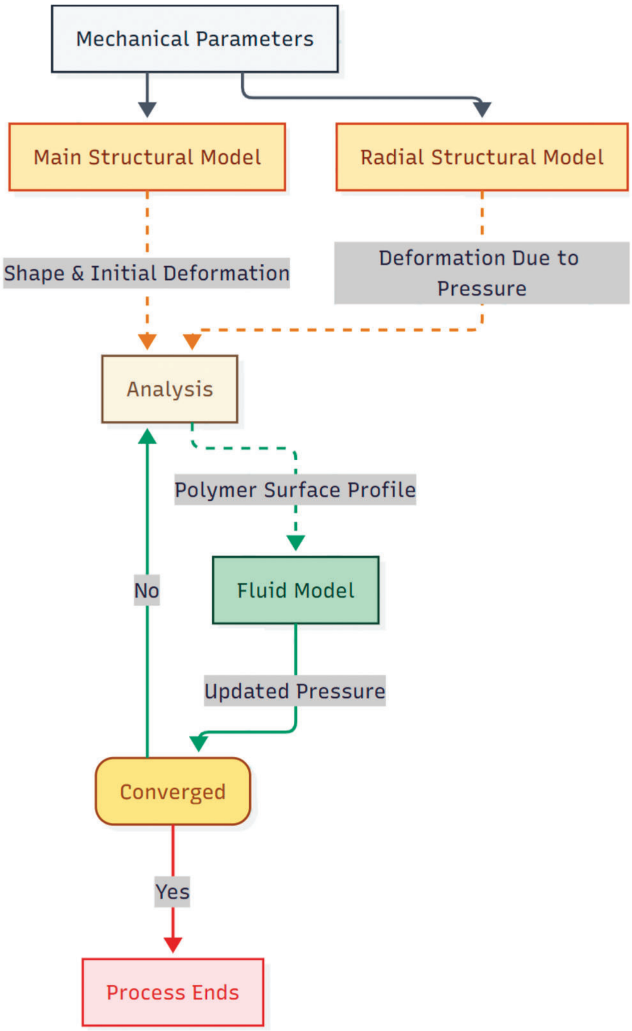

Figure 2: Fluid-structural coupling process flowchart.

boundaries are established. The following sections provide a detailed description of the fluid model.

3.3.1 *Assumptions*

The following have been assumed for the simulations:

- Air and ink are treated as immiscible phases.
- Since the density of air is three orders of magnitude smaller than that of ink, the momentum of air is negligible compared to that of ink, provided their velocities are similar.
- Among several cavities on the textured-surface roller, a single cavity (cell) is considered in the simulation domain. This assumption is justified by (i) the negligible effect of the surrounding air on the ink flow, and (ii) the fact that ink exists as patches within the cavities, with no noticeable interactions between ink patches in neighbouring cavities.
- While ink remains trapped inside the cavity, the surrounding air has no effect on the ink transfer process. Therefore, as long as the flow between the inside and outside of the cavity is blocked, the composition of the fluid outside the cavity becomes irrelevant.
- The flow is assumed to be laminar. For a single-phase fluid around a rotating disc, the laminar flow condition is given by $Re = Vr/\nu < 3.25 \times 10^5$, where Re is the Reynolds Number, V is the linear velocity at the disc's outermost surface, r is the disc radius, and ν is the kinematic viscosity (Dmitrenko, 2021). While determining a laminar flow condition for a two-phase fluid is complex, using the viscosity of the less-viscous phase (air) in the calculation of Re provides a conservative limit. Based on the physical values provided in Section 5, the Reynolds Number is sufficiently low, justifying the laminar flow assumption.
- Heat generation effects are negligible.

3.3.2 *Governing equations*

The fundamental equations for the conservation of mass and momentum are as follows:

$$\frac{\partial \rho}{\partial t} + \nabla \cdot (\rho \mathbf{u}) = 0 \tag{3}$$

$$\frac{\partial}{\partial t}(\rho \mathbf{u}) + \nabla \cdot (\rho \mathbf{u}\mathbf{u}) = -\nabla p + \nabla \cdot (\overline{\overline{\tau}}) + \rho \mathbf{g} + \mathbf{F} \tag{4}$$

where ρ represents the density, $\mathbf{u}$ the velocity vector, $\overline{\overline{\tau}}$ the deviatoric stress tensor (Kundu & Cohen, 2002), $\rho\mathbf{g}$ is the gravitational force, and $\mathbf{F}$ any other external body force.

In the volume of fluid (VOF) method, a quantity α_q is defined to denote the local volume fraction of phase q. The equation below, derived from the continuity equation, is solved for the air phase:

$$\frac{\partial}{\partial t}(\alpha_a \rho_a) + \frac{\partial}{\partial x_j}(\alpha_a \rho_a u_j) = \dot{m}_{ia} - \dot{m}_{ai} \tag{5}$$

where j denotes x, y, or z coordinates. For the ink phase, we have simply $\alpha_i = 1 - \alpha_a$.

When the Eulerian method is used as the multi-phase model, the equations for mass and momentum conservation take more complex forms, as shown below:

$$\frac{\partial}{\partial t}(\alpha_q \rho_q) + \frac{\partial}{\partial x_j}(\alpha_q \rho_q u_j) = \sum_{p=1}^{n} (\dot{m}_{pq} - \dot{m}_{qp}) \tag{6}$$

and

$$\frac{\partial}{\partial t}(\alpha_q \rho_q u_{q,i}) + \frac{\partial}{\partial x_j}(\alpha_q \rho_q u_{q,i} u_{q,j}) = -\alpha_q \frac{\partial p}{\partial x_i} + \frac{\partial}{\partial x_j}(\overline{\overline{\tau}}_j) + \alpha_q \rho_q g_i + \sum_{p=1}^{n} (R_{i,pq} + \dot{m}_{pq} u_{pq,i} - \dot{m}_{qp} u_{qp,i}) + F_{q,i} + F_{lift,q,i} + F_{wl,q,i} + F_{vm,q,i} + F_{td,q,i} \tag{7}$$

where n is the number of phases in the domain, $u_{q,i}$ is the velocity component i for the phase q, $u_{qp,i}$ is the relative velocity between phases p and q in the direction i, $\overline{\overline{\tau}}$ is the phase stress-strain tensor, and $R_{i,pq}$ is an interaction force between phases related to various effects such as friction, pressure, and cohesion. $F_{q,i}$ is the external body force, and $F_{lift,q,i}$, $F_{wl,q,i}$, $F_{vm,q,i}$, and $F_{td,q,i}$ are forces relating to lift, wall lubrication, virtual mass, and turbulent dispersion, respectively.

The ANSYS Fluent 2021 R1 Theory Guide (ANSYS & Inc., 2021) provides further details about the governing equations, for the basic equations (p. 3), VOF method (pp. 574–578), and Eulerian method (pp. 623–695).

3.3.3 *Contact handling and meshing*

In the fluid model, when the elastic surface comes into contact with the textured-surface roller, a small gap is introduced to prevent mesh clashes, ensuring that the surfaces do not physically touch. This gap is controlled to maintain realistic fluid conditions within the cavity. As a result, the deformed body's profile closely aligns with the structural analysis results while maintaining a high-quality mesh. During the contact, the gap is filled with a high-viscosity auxiliary fluid to prevent fluid leakage and isolate the cavity's inside from the outside environment.

A Lagrangian approach is employed in which the mesh rotates with the rigid roller. Any part of the elastic surface of the domain that is not in contact with the rigid roller rotates in alignment with the elastic roller; otherwise, it is considered to be attached to the surface of the rigid body and moves with the rest of the domain. This results in the deformation of the elastic surface to conform to the rigid roller surface. Nonetheless, in the areas of the cavity, it also experiences a calculated penetration into the cavity.

To create a gap between the roller surfaces, a virtual surface is introduced on top of the rigid roller with a distance equal to the prescribed gap, named 'top-surface gap'. Each part of the elastic roller surface undertakes five stages during the simulation, as shown in Figure 3A:

i) *Outside contact.* This consists of the upstream and downstream regions where the elastic roller is not in contact with the virtual surface of the rigid roller.
ii) *In-real contact.* Region where the actual surface of the rigid roller makes contact with the elastic roller surface.
iii) *In-virtual contact.* Two areas located between the upstream and downstream regions of outside and the in-real contact regions.

As illustrated in Figure 3B, the in-virtual contact area conforms to the rigid roller surface with a prescribed gap, top-surface gap.

At each time-step, the cell walls on the rigid body surface are projected onto the elastic body surface to determine the position of contact points on the elastic surface. Figure 4 shows a schematic of a cavity, highlighting the contact and near-contact areas. Areas of the elastic body surface predicted to touch the rigid roller surface are named as 'contact area', areas with a distance less than a prescribed 'side gap' are called 'near contact area', and areas predicted to fall on the cavity (with distances to the top surface greater than the side gap) are called 'on the cavity area'.

Accordingly, the motions and deformations are applied in the following manner:

- Throughout the simulation, a rigid mesh motion is applied to the entire domain based on the rotations of the rigid roller.
- When any part of the elastic body is in the outside contact region, the rigid roller's rotation is omitted, but that of the elastic roller is applied.
- In-virtual contact, any part of the elastic surface reaching a contact area is deformed in the direction opposite to the centre of the rigid body, positioning it to the virtual surface of the rigid roller to preserve the prescribed gap. Any part reaching a near-contact area is gradually displaced towards the virtual surface based on its distance from the contact area. This creates a prescribed gap between the elastic body and the side walls of the cavity.
- In real contact, any part of the elastic body surface located at the top of the cavity undergoes deformation based on the elastic surface profile determined from the structural analysis.

Since rigid mesh motion is applied to the domain, all elements move with the geometry based on the rigid roller's motion. Remeshing is implemented to update the mesh in line with the relative motion of the rotating surfaces and the deformations of the elastic body, representing a conformal mesh approach. Tetrahedral elements are chosen, and mesh smoothing is applied, primarily to expand the domain when the bodies separate automatically. The spring-based smoothing method is used, as it accommodates geometry modifications and ensures good mesh quality at a reasonable computational cost.

3.3.4 *Configuration of fluid model solver*

A suitable multi-phase model is essential for simulating air and ink transport within the domain. The VOF method is reasonably accurate when the ink and air remain segregated and are not dispersed within the domain. It is computationally efficient, making it suitable for the early stages of the process. However, once contact begins to open and the ink starts to break down, mixing with air, a more accurate, though computationally expensive, method is required. In these later stages, the Eulerian method is employed to provide improved accuracy.

For the Eulerian model, the multi-fluid VOF submodel is used with a Courant Number of 0.25. The interface is modelled as Sharp/Dispersed, and the sub-time-step calculation uses the Hybrid method. For the phase interactions, the force is calculated using the Schiller–Naumann model for the drag coefficient, with no model applied for the lift coefficient and wall lubrication. The virtual mass coefficient and the interfacial area are treated using particle formulation. To avoid excessive computational time, no population balance model is used in the simulations.

In all cases, continuum surface stress (ANSYS & Inc., 2021; Brackbill *et al.*, 1992) is used for modelling surface tension force.

The coupled scheme is adopted for the pressure–velocity coupling. Spatial discretization for gradients, pressure, momentum, and volume fraction is applied with least-squares cell-based, second- and first-order upwind, and compressive schemes, respectively. Ink is modelled as an incompressible liquid. For air, the compressibility is considered a function of pressure, with a bulk modulus based on isothermal flow for an ideal gas.

4. Assessment of the Fluid Model With a Simplified Approach

To the best of the authors' knowledge, no experimental data are available to directly quantify the process of ink transfer from a cavity to a flexible, penetrating surface. Consequently, the fluid model is validated using a simplified liquid transfer process between two parallel plates. This approach is chosen due to its well-established theoretical framework and availability of experimental data for comparison. Additionally, although the flat-plate model does not replicate the geometrical and dynamic complexities of roller-based systems, it captures the fundamental ink-splitting mechanics, such as capillary forces, film splitting dynamics, and ink viscosity effects, that govern ink transfer. These principles are directly applicable to roller-based processes.

The analysis focuses on the liquid pick-up (or transfer ratio), defined as the proportion of liquid carried by the upper plate after separation relative to the total liquid volume. The validation simulations involve placing a droplet on a stationary plate at the bottom (depicted in Figure 5). The upper plate approaches and contacts the droplet. When the distance between the plates becomes a specified value, the upper plate halts momentarily before moving away from the lower plate. The gravity is ignored, and the liquid material is water. The parameters used in this study include the droplet volume is 0.26 mm^3, the upper plate approach and leaving speeds of 2.5 mm/s, and the pause duration of the upper plate before movement is 2.5 ms.

A mesh sensitivity study was conducted for three cases by progressively doubling the number of elements and computing the liquid pick-up for each. A 9% or less difference in results be-

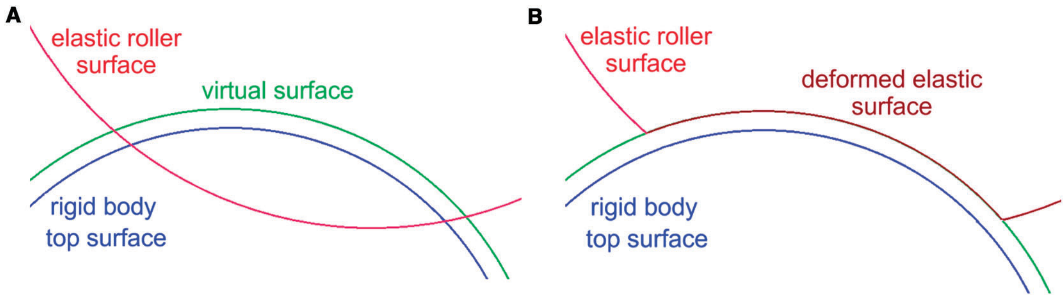

Figure 3: A schematic illustrating the concept of virtual surfaces with exaggerated scales. (A) The surfaces of the rollers and the virtual surface before any deformations are applied. The distance between the rigid body top surface (blue circle) and the virtual surface (green circle) is referred to as the 'top surface gap'. The areas between the blue and green circles represent the 'in-virtual contact' areas. The portion of the elastic roller surface (red circle) enclosed within the blue circle is the 'in-real contact' area. (B) The state after deformations due to roller interference; note that deformations from the penetration of the elastic surface into the cavities are not depicted. The top-surface gap is intentionally exaggerated for clarity, and the image is entirely schematic and not to scale.

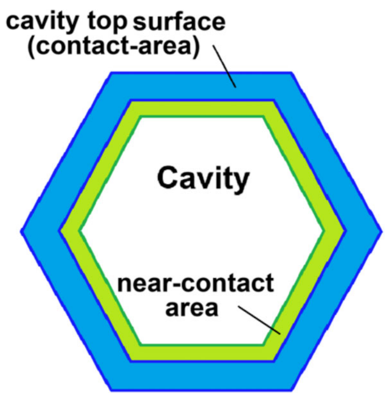

Figure 4: A schematic of a cavity viewed from above, illustrating the contact and near-contact areas. The figure is not to scale, and the widths of the areas are exaggerated for clarity.

tween consecutive cases was deemed acceptable. An intermediate mesh with an initial 3.7 million elements was found appropriate. A subsequent time-step size sensitivity analysis justified using $\Delta t = 5 \times 10^{-6}$ s before liquid breakup and $\Delta t = 2 \times 10^{-6}$ s during and after the breakup.

The theoretical formulation assumes a quasi-static process, maintaining internal physical equilibrium for the system throughout. The liquid pick-up is calculated using the following equations (Ghadiri *et al.*, 2011; Kang *et al.*, 2009):

$$tr = f(\alpha) / (f(\alpha) + f(\beta)) \tag{8}$$

where, α and β represent the surface contact angles of the liquid droplet with the upper and lower plates, respectively. For the axisymmetric case in which a plate is stationary and the other plate moves, the function $f(x)$ is formulated as follows (Ghadiri *et al.*, 2011; Kang *et al.*, 2009):

$$f(x) = -\pi/2 + x + 2\cos(x) - \sin(x)\cos^3(x) - \cos^3(x)/3 \times (x \text{ is replaced by } \alpha \text{ or } \beta) \tag{9}$$

Equation 8 reflects the balance of geometric and physical effects at the contact line, where the contact angle influences liquid transfer. The terms account for the angular inclination of the droplet at the solid–liquid interface ($-\pi/2 + x$), curvature of the meniscus and its vertical projection ($2\cos(x)$), interaction between the droplet's slope and its horizontal deformation ($-\sin(x)\cos^3(x)$), and nonlinear corrections ($-\cos^3(x)/3$).

Figure 6 shows the simulation results obtained from the present model, along with the theoretical values for axisymmetric plate motion and experimental data from Kang *et al.* (2009).

The simulation results from the present model are generally lower than the theoretical values but higher than the experimental measurements by Kang *et al.* (2009). A good agreement is observed between the simulation results and both the theoretical and experimental data across most ranges of contact angles. It should be noted that while the flat-plate model does not replicate the geometrical and dynamic complexities of roller-based systems, it captures the fundamental ink-splitting mechanics that govern ink transfer. These principles, such as capillary forces, film splitting dynamics, and ink viscosity effects, are directly applicable to the roller-based process.

5. Results and Discussion

5.1 Parameters for the case study

The process of ink transfer from a cavity to a flexible penetrating surface is studied for a case using the proposed modelling approach. The cavity, which is hexagonal in shape, is located on the surface of the rigid roller and is initially filled with 85% ink at the bottom. Other physical parameters are listed in Table 1. The physical parameters used in the simulation. The values are dominantly selected from practical values. The cavity depth and opening assumed for simulation are consistent with values reported in Valdec *et al.* (2021) and Verona (2005). While the optimal range for interference is typically 20–150 μm (Valdec et al., 2021), low interference values can be advantageous for specific printing conditions (Bould *et al.*, 2004), particularly where minimal pressure is required to achieve a 'kiss impression' (Deamon, 2014; Luminite Products Corp., 2025). This choice also facilitated smoother structural simulations. Literature predominantly provides a single value for ink-anilox roller wettability, while the wettability of the roller top surface may differ from that of cell surfaces. The ink-anilox cell (cavity surface) contact angle used in this study is within the range provided in (Verona, 2005). Similarly, ink-polymer contact angles of 20° are documented in (Sant'Ana *et al.*, 2022).

A viscosity of 0.5 Pa·s was employed for the auxiliary fluid during the contact between the rollers. This value was selected based on observations from a series of simulations with different auxiliary fluid viscosities, ranging from 10 times the viscosity of air to 5 Pa·s. The study revealed that for viscosities exceeding 0.15 Pa·s, the results became insensitive to viscosity, as no significant motion of the auxiliary fluid from the cavity side

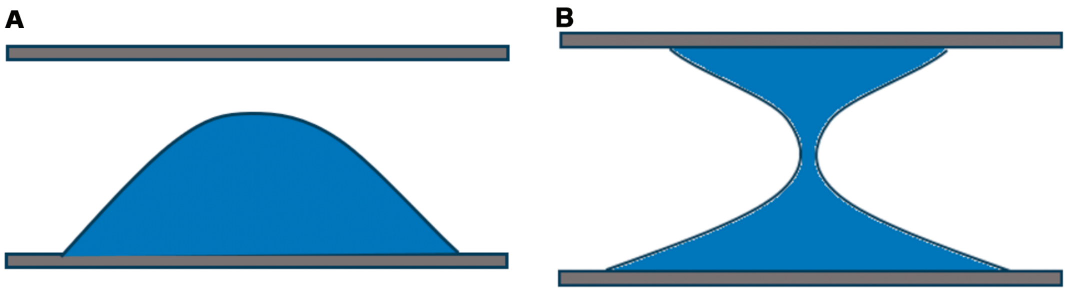

Figure 5: A demonstration of droplet split-up between flat plates: (A) initial conditions, and (B) while the upper plate moves upward.

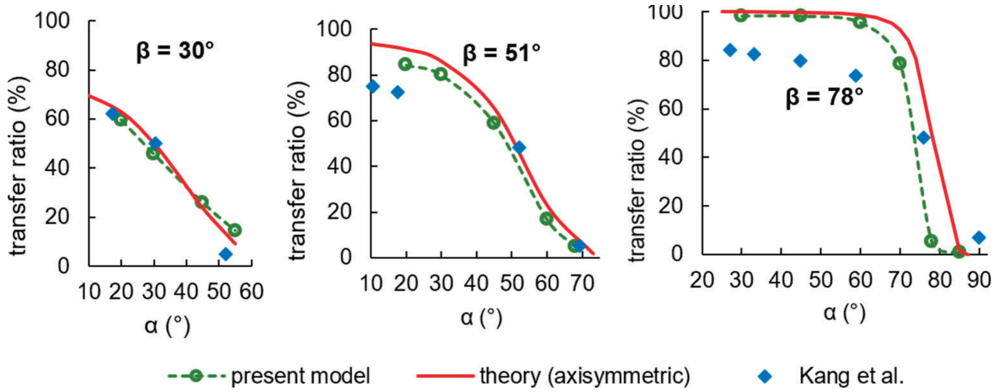

Figure 6: Liquid pick-up (%) between flat plates obtained by simulations compared with the experimental data and the theory for different contact angles.

Table 1: The physical parameters used in the simulation.

Parameter	Value	Unit	Source
Linear speed on the roller surfaces	5	m/s	Selected based on Izdebska (2016) and Kumar (2015)
Rigid roller radius	8	cm	Selected based on Cherry & Allen (2007)
Elastic roller radius	10	cm	Selected based on Kumar
Interference between rollers	15	μm	Assumed
Ink density	1050	kg/m^3	Johnson (2008)
Ink viscosity	0.075	Pa·s	Johnson (2008)
Ink-air surface tension	0.030	N/m	Johnson (2008)
Ink contact angle with cavity surface	90	deg	Assumed
Ink contact angle with polymer	20	deg	Assumed
Cavity opening	30	μm	Assumed
Cavity depth	12.5	μm	Assumed

to the outside was observed. However, excessively high viscosities introduced convergence difficulties during simulations. The choice of 0.5 Pa·s ensures the auxiliary fluid effectively replicates the no-leakage condition while maintaining computational stability.

The transition from the VOF to the Eulerian model was performed shortly after the point of maximum penetration ($t = 0.24$ ms), where the ink–air interface begins to fragment and mix. This timing ensures the Eulerian model's computational advantages are utilized during the critical breakup and mixing phases to improve the accuracy of the results.

5.2 Verification

A comprehensive verification study has been conducted to assess the sensitivity of the results to the mesh and time-step sizes. This verification is particularly important given that the available benchmarks used for validation have significant differences from the contact-based printer system being simulated here.

For this purpose, a series of runs were conducted with different mesh sizes (mesh sensitivity study) and time-steps (temporal discretization verification). The simulation parameters are broadly similar to the physical parameters outlined in Table 1, and the model set-up is the same as in the main simulations. However, to reduce the computational costs, simulations were performed without using the auxiliary fluid.

In the mesh sensitivity study, runs with three different mesh sizes were conducted. Due to dynamic remeshing, the number of elements varies during the runs. The ratio of the element's counts remains almost unchanged by prescribing suitable length-scales for the meshing in key areas, such as the polymer and cavity surfaces. The number of elements during the runs is reported in Figure 7. Figure 8 illustrates the ink pick-up (transfer ratio) for each case. Although the number of elements for the intermediate mesh

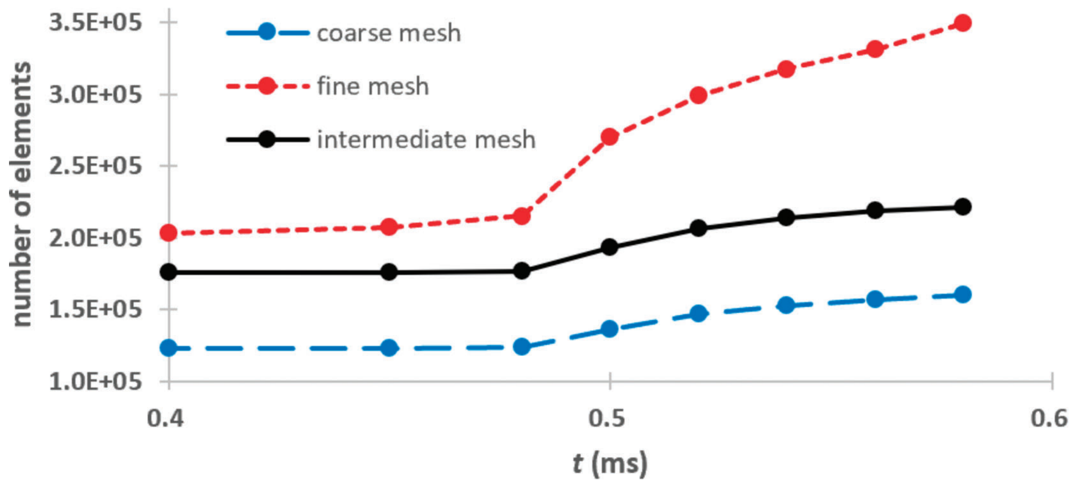

Figure 7: Total number of cells in the domain for different mesh-size scenarios.

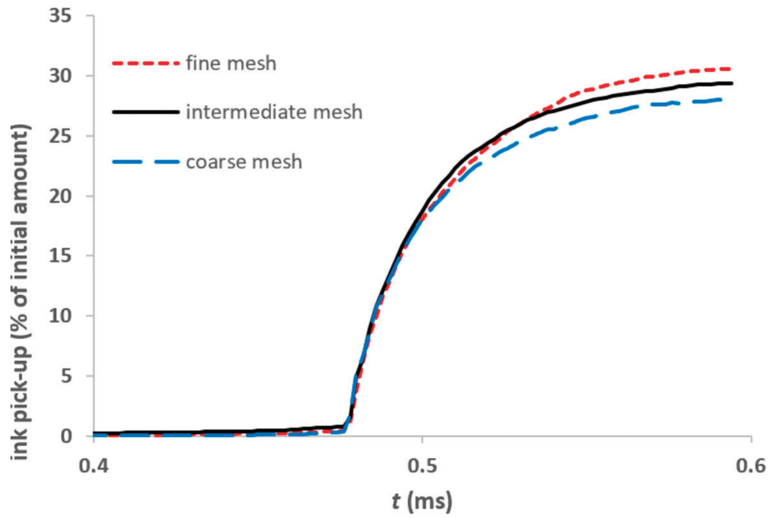

Figure 8: Ink pick-up curves (% of initial ink inside the cavity) for different mesh-size scenarios.

at the start of separation (when the number of elements begins to increase) is mostly closer to the coarse mesh, the curves for the intermediate and fine meshes are sufficiently close to each other, with less than a 4% deviation in the final pick-up values between the different meshes. Based on calculations using Richardson extrapolation (Andersen, 2014), the pick-up values exhibit a deviation of less than 15% between the intermediate and exact solutions. Therefore, the meshing parameters for the intermediate case are used for the simulations. It should be noted that the minimum sizes prescribed for the gaps influence the mesh resolution, and comparability between them should be maintained. A coarse mesh with overly small gaps leads to poor mesh quality. Hence, for the mesh independence study, we applied gap sizes compatible with the coarse case and used the same values for all cases. However, for the simulations, since we use the intermediate mesh, a slightly smaller gap is used.

For the justification of the temporal discretization, the intermediate mesh was used to conduct simulations with four different time-steps. Some parameters differed from those used in the mesh independence study. The general time-step values were 4.5×10^{-8}, 1.5×10^{-8}, 1.0×10^{-8}, and 6.0×10^{-9} seconds. However, on occasions when divergence occurred, slightly smaller time-steps were temporarily employed to navigate past the point of divergence. Based on the results for ink pick-up at different time-steps (Figure 9), the 'intermediate' time-step produced results close to those of the 'small' time-step case. Therefore, a time-step of 1.0×10^{-8} s was chosen for the main simulation.

5.3 Ink-transfer process

The structural analysis was conducted using a 0.3-mm-thick polymer. The deformation behaviour was considered linear, with Young's modulus and Poisson's ratio equal to 20 MPa and 0.494, respectively. It was found that the polymer's penetration into the anilox cavity occurs primarily near the cavity walls, resulting in a sharp profile at the walls and a nearly flat profile in the middle during full penetration. The pressure applied by the locked fluid reduces the degree of penetration and becomes noticeable at pressures higher than 5×10^5 Pa.

The ink transfer process is further analysed using Figures 10–13. Figure 10 shows the ink distribution in the domain along with cross-sections of the cavity. Figure 11 provides 3D views of the ink distribution during the breakup. Figure 12 illustrates a scaled conceptual timeline of the main stages of ink transfer. Figure 13 presents variations in the average air pressure inside the cavity

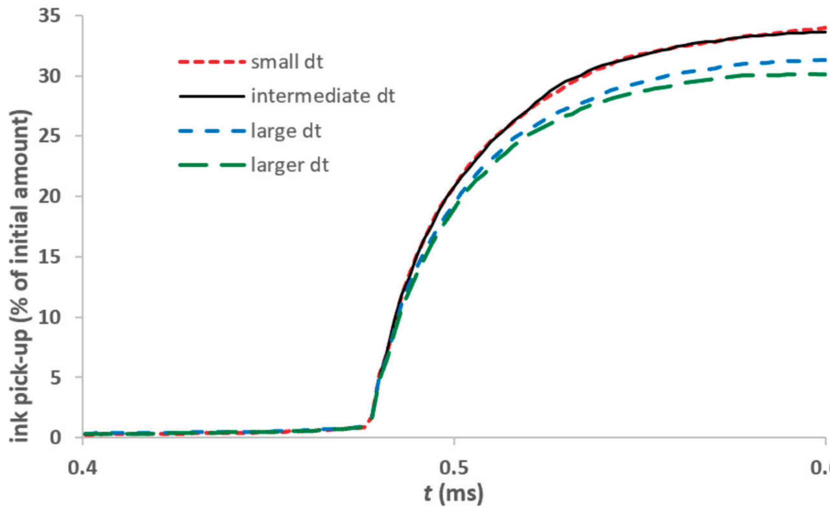

Figure 9: Ink pick-up curves (% of initial ink inside the cavity) for different time-steps. General values for the time-steps from the smallest to the largest are 4.5*e*−8, 1.5*e*−8, 1.0*e*−8, and 6.0*e*−9 s, respectively.

throughout the process. The entire process, from the start of contact to the end of the ink breakup, takes about 0.7 ms. The figures illustrate the following stages in the course of ink transfer between the rollers:

A. *Pre-contact.* In this stage, the ink resides in the bottom of the cavity under near-steady conditions. The curvature of the ink surface is controlled by surface tension, which depends on the wettability properties of the surface. Surface tension directly affects the alignment of the surface in the vicinity of the cavity wall. If the cavity opening is small, this effect can extend throughout the cavity. In the studied case, the ink surface exhibits a convex shape, but if the walls are sufficiently hydrophilic, the surface may become concave.
B. *Development of contact.* Contact with the polymer begins at the downstream edge of the cavity and quickly progresses toward the upstream. During this stage, while the polymer surface approaches the cavity, a stream of fluid exits the cavity until contact is fully established. At this point, the penetration of the polymer into the cavity is trivial.
C. *Isolation.* During this stage, the contact is fully closed. Due to the flexibility of the polymer, shortly after complete contact, the fluid inside the cavity becomes isolated from the external environment, halting mass, and momentum exchange. The pressure inside the cavity becomes disconnected from the outside. Depending on the initial volume of ink inside the cavity, a certain amount of air may also be trapped. Because the ink is highly incompressible, the penetrating material occupies a portion of the space previously filled by air. As penetration progresses, the cavity space decreases, compressing the air and increasing the pressure. The peak pressure is reached at maximum penetration, and is influenced by the geometrical interference between the rollers and the volume of the trapped air. If a small amount of air is trapped, pressure rises more sharply to a higher peak. Once maximum penetration is reached, the polymer surface begins to leave the cavity space. The rate of polymer penetration and departure is lower around the point of maximum penetration, dictated by geometry and supported by the pressure rise. The pressure acts against penetration, slowing its speed and magnitude. As a result, the trapped fluid mixture approaches stability, and ink maintains coherence by pushing air along the polymer surface. Small air bubbles will likely merge into larger bubbles. By the end of this stage, the pressure nearly returns to its value at the beginning of isolation.
D. *Contact opening.* The polymer surface starts to leave the rigid roller surface. During this stage, the pressure inside the cavity shifts toward equilibrium with the external environment.

Ink breakup. As the polymer surface leaves the cavity, it pulls the attached ink along. From this point, there is a contest between the forces acting on the ink. While gravity pulls ink as the denser fluid downward, the ink attached to the polymer surface is pulled upward. This interplay of opposing forces reduces the volume fraction of ink between the surfaces, making the ink core thin and narrow. In contrast, the cohesion stress tends to maintain the ink as a unified mass. Due to the expansion of the space between the surfaces, the pressure drops, creating a stream of air that further narrows the ink core. Eventually, the thinnest points of the ink patch rupture. The ink patch attached to the polymer continues to move with it, while small droplets that do not sufficiently adhere may separate and fall. An ink pick-up rate of 27% has been calculated.

Figure 12 illustrates the timeline of the ink transfer process, detailing key stages from pre-contact to ink breakup. The graph visually maps the sequential progression of events, highlighting the temporal relationship between stages and their role in the overall process.

Due to the lack of detailed, condition-specific benchmark data regarding the amount of ink transferred from the anilox roller to the flexo-plate roller, only broad ranges reported in the literature can be referenced for this process. Transfer rates of 30%–60% (Aleksashenko, 2007) and 25%–50% (Madsen, 2014) have been cited by academic and industrial sources. Given that the simulation conditions in this study are representative rather than precisely matching industrial practice, the calculated value of 27% is consistent with the lower end of these reported ranges. This agreement supports the plausibility of the simulation results, given the inherent variability and sensitivity of ink transfer to process parameters.

For air treated as an ideal gas, the pressure strongly depends on the volume of the isolated air. Therefore, the pressure curve

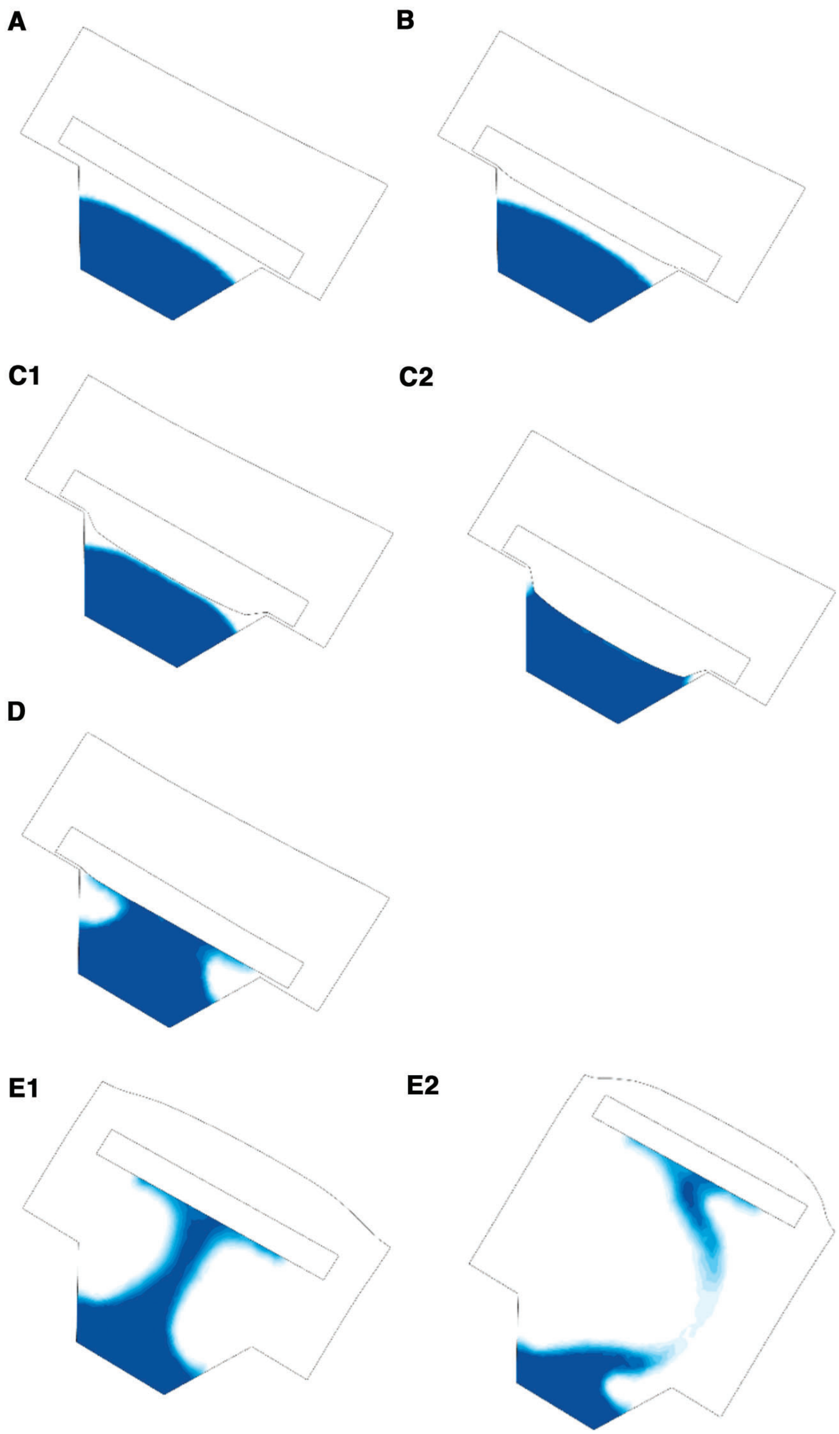

Figure 10: Cross-section views of the cavity showing ink at various stages of ink transfer between rollers based on contact conditions and configuration of ink: (A) pre-contact, (B) contact development, (C) isolation; C1: penetration, C2: maximum penetration, (D) contact opening, and (E) ink breakup; E1: thinning, E2: rupture.

reflects the geometrical volume of the isolated cavity minus the trapped ink volume. The pressure starts to rise as the contact begins to develop (point b). As the polymer penetration progresses (point c1), the rate of pressure increase accelerates due to the compression of the air volume. This rate eventually slows down until maximum penetration is reached (point c2), at which point the pressure also peaks. Afterwards, the pressure gradually decreases as the penetration reduces, following a curve similar to the penetration phase. Once the contact fully opens (after point d), the pressure returns to its original value, equal to the external pressure.

During the final rupture stage, surface tension plays a significant role in controlling cavity separation, acting in competition with viscous resistance during compression. While this work focuses on qualitative trends, quantification of these effects using dimensionless measures such as the capillary number and interface-shape evolution is considered for future studies.

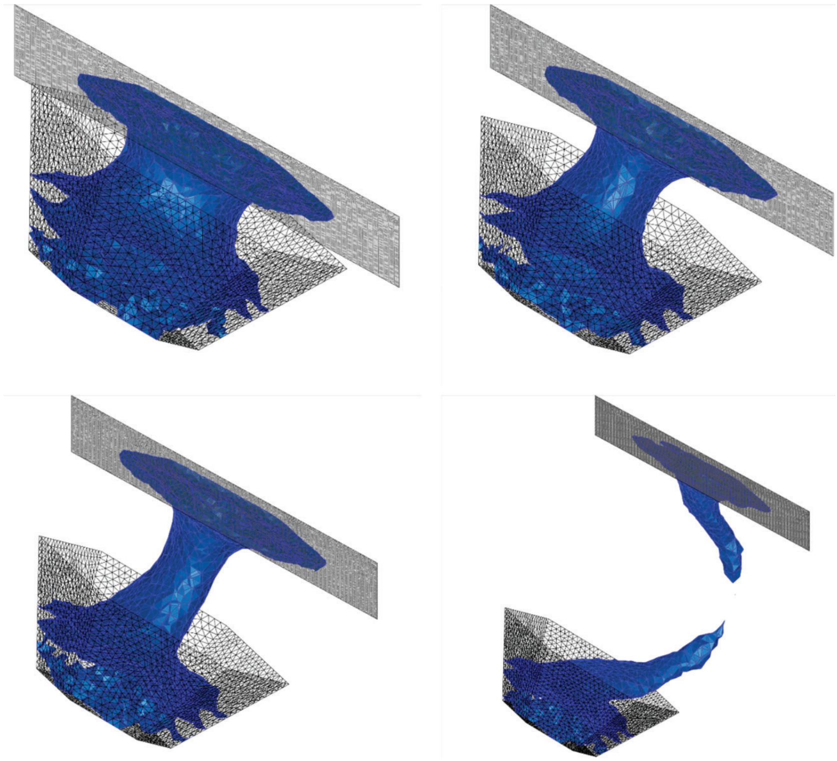

Figure 11: 3D views of ink-break-up.

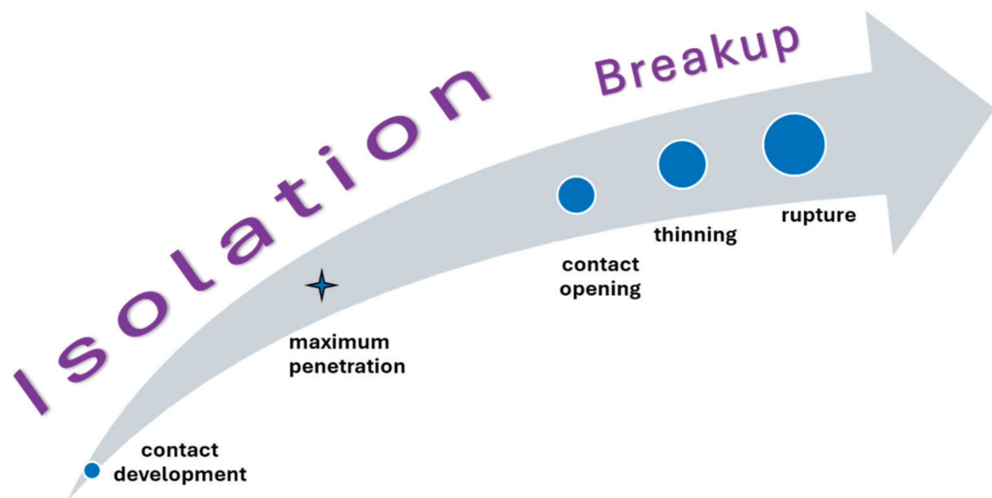

Figure 12: A scaled conceptual timeline graph illustrating the progression of ink-transfer stages.

6. Conclusions

An approach is proposed herein for simulating fluid flow under the influence of moving structures with overlapping walls, where a portion of the fluid is trapped between the surfaces of the structures. The developed approach is applied to simulate ink transfer between two rollers in contact-based printing systems, particularly in flexographic printers, where there is a considerable penetration.

To maintain continuity within the fluid domain during the process, the proposed approach prescribes a small gap between the physically overlapping moving walls. This gap is filled with a high-viscosity fluid to replicate actual attached surfaces. The multiphase model comprises compressible air and incompressible ink as the primary phases, along with the additional high-viscosity fluid, which is present only during the period when the surfaces are in contact, filling the space between the walls.

The results show a multi-stage process during ink transfer between the rollers: pre-contact, development of contact, isolation, contact opening, and ink breakup. Air, along with the ink, becomes trapped in the isolated space between the rollers' surfaces, and the fluids reconfigure within the space before the contact opens. Subsequently, the ink breakup process occurs, causing the ink patch to thin in the region between the roller surfaces, eventually splitting into two smaller patches, each adhering to one of the roller surfaces. These findings enhance our understanding of the

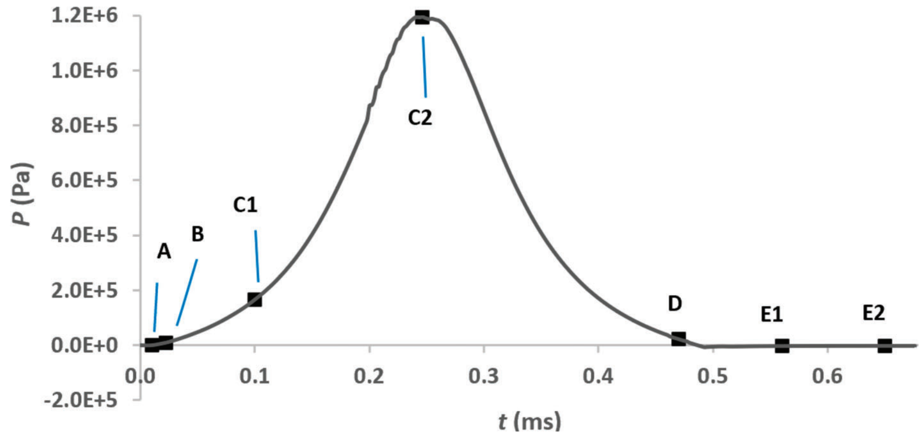

Figure 13: Average air gauge pressure variation inside the cavity at various stages of ink transfer between rollers based on contact conditions and configuration of ink: (A) pre-contact, (B) contact development, (C) isolation; C1: penetration, C2: maximum penetration, (D) contact opening, and (E) ink breakup; E1: thinning, E2: rupture.

stages involved in ink transfer between rollers, a process that has not been adequately understood. Further studies are necessary to explore the factors influencing the location of the ink breakup.

This study acknowledges a few limitations associated with its framework. The analysis assumes a single cavity within the textured surface of the roller, neglecting potential interactions between neighbouring cavities that may influence polymer deformation. Additionally, the effects of heat generation, particularly during structural contact, are not accounted for in the current model. A loose fluid-structural coupling approach has been implemented, leaving room for enhanced accuracy through a stronger coupling approach. With a more robust structural model, particularly for addressing the challenges of modelling structure-to-structure contact, the primary and radial structural simulations could be integrated into a single model incorporating roller contact and fluid pressure. The parameters used in the simulations could be refined to better align with practical conditions, and the absence of experimental data prevents thorough validation of the model. Addressing these limitations in future work could significantly improve the reliability and applicability of the findings.

The established simulation framework can be utilized in FSCI applications involving fluid entrapment due to the re-attachment of structural surfaces, particularly in cases of noticeable structural deformation caused by the use of elastic materials or significant loading. These include a variety of scenarios requiring specific scrutiny, such as the study of the dynamics of rotating tyres on wet, non-smooth surfaces, elastic clutch systems, and the fastening process of gasketed flange connections.

Conflicts of Interest

The authors declare that they have no known competing financial interests or personal relationships that could have appeared to influence the work reported in this paper.

Author Contributions

Mehdi Seddiq: Investigation, Methodology, Writing—original draft, Writing—reviewing and editing, Software, Visualisation, Conceptualisation. **Phillip Taylor**: Visualisation, Data curation, Writing- literature review, Writing- review & editing. **Leon Newton**: Investigation. **Martin Sharp**: Funding acquisition, Project administration, Writing—reviewing and editing. **Mehdi Seddighi:** Funding acquisition, Project administration, Conceptualisation, Supervision, Writing—reviewing and editing.

Funding

This research was supported by Innovative UK (TS/S015906/1). The authors would also like to thank EPSRC for the computational time made available on the UK supercomputing facility ARCHER2 via the UK Turbulence Consortium (EP/X035484/1).

References

Abbott, S. (2018). *Printing Science: Principles and Practice* (pp. 179). Retrieved July 18, 2024, fromwww.stevenabbott.co.uk

Ager, C., Schott, B., Vuong, A. T., Popp, A., & Wall, W. A. (2019). A consistent approach for fluid-structure-contact interaction based on a porous flow model for rough surface contact. *International Journal for Numerical Methods in Engineering*, **119**, 1345–1378. https://doi.org/10.1002/nme.6094

Ahmed, D. H., Sung, H. J., & Kim, D.-S. (2011). Simulation of non-Newtonian ink transfer between two separating plates for gravure-offset printing. *International Journal of Heat and Fluid Flow*, **32**, 298–307. https://doi.org/10.1016/j.ijheatfluidflow.2010.06.011

Aleksashenko, M.. Experimental research of anilox rolls parameters with raster electronic microscope. In: Wissenschaft und Forschung Verlag für (ed.), *Proceedings of the 2nd International Student Conference on Print and Media Technology: Printing Future Days 2007*. Chemnitz, Germany, 2007, 133.

Andersen, J. (2014). *Systematic Variations of Parameters Affecting Waterjet-hull Interaction. Master's Thesis*. Chalmers University of Technology. (X-14/301).

ANSYS, Inc. (2021). *ANSYS Fluent Theory Guide (Release 2021 R2)*. Canonsburg, PA: ANSYS, Inc..

Astorino, M., Gerbeau, J.-F., Pantz, O., & Traoré, K.-F. (2009). Fluid–structure interaction and multi-body contact: Application to aortic valves. *Computer Methods in Applied Mechanics and Engineering*, **198**, 3603–3612. https://doi.org/10.1016/j.cma.2008.09.012

Banks, J. W., Henshaw, W. D., Schwendeman, D. W., & Tang, Q. (2018). A stable partitioned FSI algorithm for rigid bodies and incompressible flow in three dimensions. *Journal of Computational Physics*, **373**, 455–492. https://doi.org/10.1016/j.jcp.2018.06.072

Basting, S., Quaini, A., Čanić, S., & Glowinski, R. (2017). Extended ALE method for fluid–structure interaction problems with large structural displacements. *Journal of Computational Physics*, **331**, 312–336. https://doi.org/10.1016/j.jcp.2016.11.043

Bavo, A. M., Rocatello, G., Iannaccone, F., Degroote, J., Vierendeels, J., & Segers, P. (2016). Fluid-structure interaction simulation of prosthetic aortic valves: Comparison between immersed boundary and arbitrary lagrangian-eulerian techniques for the mesh representation. *PLoS ONE*, **11**, e0154517. https://doi.org/10.1371/journal.pone.0154517

Benra, F.-K., Dohmen, H. J., Pei, J., Schuster, S., & Wan, B. (2011). A comparison of one-way and two-way coupling methods for numerical analysis of fluid-structure interactions. *Journal of Applied Mathematics*, **2011**, 1–16. https://doi.org/10.1155/2011/853560

Borazjani, I. (2013). Fluid–structure interaction, immersed boundary-finite element method simulations of bio-prosthetic heart valves. *Computer Methods in Applied Mechanics and Engineering*, **257**, 103–116. https://doi.org/10.1016/j.cma.2013.01.010

Borazjani, I., Ge, L., Le, T., & Sotiropoulos, F. (2013). A parallel overset-curvilinear-immersed boundary framework for simulating complex 3D incompressible flows. *Computers & Fluids*, **77**, 76–96. https://doi.org/10.1016/j.compfluid.2013.02.017

Borazjani, I., Ge, L., & Sotiropoulos, F. (2008). Curvilinear immersed boundary method for simulating fluid structure interaction with complex 3D rigid bodies. *Journal of Computational Physics*, **227**, 7587–7620. https://doi.org/10.1016/j.jcp.2008.04.028

Bould, D. C., Claypole, T. C., & Bohan, M. F. J.. (2004). An investigation into plate deformation in flexographic printing. *Proceedings of the Institution of Mechanical Engineers, Part B: J. Engineering Manufacture*, **218**, 1499 –1511.

Brackbill, J. U., Kothe, D. B., & Zemach, C. (1992). A continuum method for modeling surface tension. *Journal of Computational Physics*, **100**, 335–354. https://doi.org/10.1016/0021-9991(92)90240-Y

Calandrini, S., & Aulisa, E. (2019). Fluid-structure interaction simulations of venous valves: A monolithic ALE method for large structural displacements. *International Journal for Numerical Methods in Biomedical Engineering*, **35**, e3156. https://doi.org/10.1002/cnm.3156

Cao, Y., Nie, S., & Wu, Z. (2017). Numerical simulation of parachute inflation: A methodological review. *Proceedings of the Institution of Mechanical Engineers, Part G: Journal of Aerospace Engineering*, **233**, 736–766. https://doi.org/10.1177/0954410017705900

Chen, Y., & Luo, H. (2018). A computational study of the three-dimensional fluid–structure interaction of aortic valve. *Journal of Fluids and Structures*, **80**, 332–349. https://doi.org/10.1016/j.jfluidstructs.2018.04.009

Cherry, & Allen, J. (2007). *Ink release characteristics of anilox rolls*. Ph.D. Thesis. University of Wales Swansea.

De Hart, J., Baaijens, F. P. T., Peters, G. W. M., & Schreurs, P. J. G. (2003). A computational fluid-structure interaction analysis of a fiber-reinforced stentless aortic valve. *Journal of Biomechanics*, **36**, 699–712. https://doi.org/10.1016/s0021-9290(02)00448-7

Deamon, A. (2014). *Kiss Impression in Key in an Ideal Press Run*. Retrieved September 09, 2025, fromhttps://careyweb.com/kiss-impression-in-flexo-july-2014/

Dmitrenko, A. V. (2021). Determination of critical reynolds number for the flow near a rotating disk on the basis of the theory of stochastic equations and equivalence of measures. *Fluids*, **6**, 1–11. https://doi.org/10.3390/fluids6090306

Donea, J., Giuliani, S., & Halleux, J. P. (1982). An arbitrary lagrangian-eulerian finite element method for transient dynamic fluid-structure interactions. *Computer Methods in Applied Mechanics and Engineering*, **33**, 689–723. https://doi.org/10.1016/0045-7825(82)90128-1

Dong, L., Xing, J., Wu, S., Guan, X., & Zhu, H. (2021). Simulation of shear-thickening liquid transfer between U-shaped cell and flat plate. *Processes*, **9**, 838. https://doi.org/10.3390/pr9050838

Fadlun, E. A., Verzicco, R., Orlandi, P., & Mohd-Yusof, J. (2000). Combined immersed-boundary finite-difference methods for three-dimensional complex flow simulations. *Journal of Computational Physics*, **161**, 35–60. https://doi.org/10.1006/jcph.2000.6484

Ge, L., & Sotiropoulos, F. (2007). A numerical method for solving the 3D unsteady incompressible Navier-Stokes equations in curvilinear domains with complex immersed boundaries. *Journal of Computational Physics*, **225**, 1782–1809. https://doi.org/10.1016/j.jcp.2007.02.017

Gerosa, F. M. (2021). *Immersed boundary methods for fluid-structure interaction with topological changes*. Ph.D. Thesis. Sorbonne University.

Ghadiri, F., Ahmed, D. H., Sung, H. J., & Shirani, E. (2011). Non-Newtonian ink transfer in gravure–offset printing. *International Journal of Heat and Fluid Flow*, **32**, 308–317. https://doi.org/10.1016/j.ijheatfluidflow.2010.09.004

Griffith, B. E., Luo, X., McQueen, D. M., & Peskin, C. S. (2009). Simulating the fluid dynamics of natural and prosthetic heart valves using the immersed boundary method. *International Journal of Applied Mechanics*, **1**, 137–177. https://doi.org/10.1142/S1758825109000113

Ha, S. T., Ngo, L. C., Saeed, M., Jeon, B. J., & Choi, H. (2017). A comparative study between partitioned and monolithic methods for the problems with 3D fluid-structure interaction of blood vessels. *Journal of Mechanical Science and Technology*, **31**, 281–287. https://doi.org/10.1007/s12206-016-1230-2

Hsu, M. C., Kamensky, D., Bazilevs, Y., Sacks, M. S., & Hughes, T. J. (2014). Fluid-structure interaction analysis of bioprosthetic heart valves: Significance of arterial wall deformation. *Computational Mechanics*, **54**, 1055–1071. https://doi.org/10.1007/s00466-014-1059-4

Huang, W.-X., Lee, S.-H., Sung, H. J., Lee, T.-M., & Kim, D.-S. (2008). Simulation of liquid transfer between separating walls for modeling micro-gravure-offset printing. *International Journal of Heat and Fluid Flow*, **29**, 1436–1446. https://doi.org/10.1016/j.ijheatfluidflow.2008.07.002

Izdebska, J. (Flexographic printing, fundamentals and applications. In: J. Izdebska, & S. & Thomas (Eds.), *Printing on Polymers*. William Andrew Publishing, 2016, 179–197.

Joda, A., Jin, Z., Summers, J., & Korossis, S. (2019). Comparison of a fixed-grid and arbitrary lagrangian-eulerian methods on modelling fluid-structure interaction of the aortic valve. *Proceedings of the Institution of Mechanical Engineers, Part H*, **233**, 544–553. https://doi.org/10.1177/0954411919837568

Johnson, J. (2008). *Aspects of flexographic print quality and relationship to some printing parameters*. Ph.D. Thesis. Karlstad University.

Kang, H. W., Sung, H. J., Lee, T.-M., Kim, D.-S., & Kim, C.-J. (2009). Liquid transfer between two separating plates for micro-gravure-offset printing. *Journal of Micromechanics and Microengineering*, **19**, 015025. https://doi.org/10.1088/0960-1317/19/1/015025

Kipphan, H. (2001). *Handbook of Print Media: Technologies and Production Methods*: Springer.

Kumar, S. (2015). Liquid transfer in printing processes: Liquid bridges with moving contact lines. *Annual Review of Fluid Mechanics*, **47**, 67–94. https://doi.org/10.1146/annurev-fluid-010814-014620

Kundu, P. K., & Cohen, I. M. (2002). *Fluid Mechanics*(2nd edn): Elsevier.

Luminite Products Corp. (2025). *Flexo Troubleshooting Guide: 12 Common Printing Defects and How to Fix Them*. Retrieved September 12, 2025, fromhttps://cdn2.hubspot.net/hubfs/2696550/FLEXO%20TROUBLESHOOTING%20GUIDE_0B12%20COMMON%20PRINTING%20DEFECTS%20AND%20HOW%20TO%20FIX%20THEM.pdf?hsCtaTracking=b265583c-f428-4cbe-a11d-00e8edebd100%7C51b80e29-31ef-4b2c-96b7-fa1e83ef9a35

Madsen, N. (2014). *Release the Ink: Choosing Your Anilox*. Retrieved September 12, 2025, fromhttps://www.flexotechmag.com/features/release-the-ink-choosing-your-anilox

Mittal, R., Dong, H., Bozkurttas, M., Najjar, F. M., Vargas, A., & von Loebbecke, A. (2008). A versatile sharp interface immersed boundary method for incompressible flows with complex boundaries. *Journal of Computational Physics,* **227**, 4825–4852. https://doi.org/10.1016/j.jcp.2008.01.028

Mittal, R., & Iaccarino, G. (2005). Immersed boundary methods. *Annual Review of Fluid Mechanics*, **37**, 239–261. https://doi.org/10.1146/annurev.fluid.37.061903.175743

Mondal., K., & McMurtrey, M. D. (2020). Present status of the functional advanced micro-, nano-printings; a mini review. *Materials Today Chemistry*, **17**, 100328. https://doi.org/10.1016/j.mtchem.2020.100328

Nobili, M., Morbiducci, U., Ponzini, R., Del Gaudio, C., Balducci, A., Grigioni, M., & Redaelli, A. (2008). Numerical simulation of the dynamics of a bileaflet prosthetic heart valve using a fluid-structure interaction approach. *Journal of Biomechanics*, **41**, 2539–2550. https://doi.org/10.1016/j.jbiomech.2008.05.004

Park, S.-S., Jeon, Y., Cho, M., Bai, C., Lee, D.-y., & Shim, J. (2012). The FEM based liquid transfer model in gravure offset printing using phase field method. *Microsystem Technologies*, **18**, 2027–2034. https://doi.org/10.1007/s00542-012-1652-4

Peskin, C. S. (1977). Numerical analysis of blood flow in the heart. *Journal of Computational Physics*, **25**, 220–252. https://doi.org/10.1016/0021-9991(77)90100-0

Pramanik, R., Verstappen, R. W. C. P., & Onck, P. R. (2024). Computational fluid–structure interaction in biology and soft robots: A review. *Physics of Fluids*, **36**, 101302. https://doi.org/10.1063/5.0226743

Sant'Ana, P. L., Bortoleto, J. R., & Durrant, S. F. (2022). Contact angle and wettability of commercial polymers after plasma treatment. *London Journal of Engineering Research,* **22**, 13–33.

Souli, M., Ouahsine, A., & Lewin, L. (2000). ALE formulation for Fuid-structure interaction problems. *Computerl Methods in Applied Mechanics and Engineering*, **190**, 659–675. https://doi.org/10.1016/S0045-7825(99)00432-6

Spuhler, J. H., Jansson, J., Jansson, N., & Hoffman, J. (2018). 3D fluid-structure interaction simulation of aortic valves using a unified continuum ALE FEM model. *Frontiers in Physiology*, **9**, 363. https://doi.org/10.3389/fphys.2018.00363

Sun, P., Zhang, C.-S., Lan, R., & Li, L. (2021). An advanced ALE-mixed finite element method for a cardiovascular fluid–structure interaction problem with multiple moving interfaces. *Journal of Computational Science*, **50**, 101300. https://doi.org/10.1016/j.jocs.2021.101300

Takizawa, K., & Tezduyar, T. E. (2012). Computational methods for parachute fluid–Structure interactions. *Archives of Computational Methods in Engineering*, **19**, 125–169. https://doi.org/10.1007/s11831-012-9070-4

Valdec, D., Hajdek, K., Vragović, L., & Geček, R. (2021). Determining the print quality due to deformation of the halftone dots in flexography. *Applied Sciences*, **11**, 10601. https://doi.org/10.3390/app112210601

Verona, V. (2005). *Ink transfer mechanisms in flexographic printing*. Ph.D. Thesis. The Open University.

Wu, J.-T., Carvalho, M. S., & Kumar, S. (2019). Emptying of gravure cavities containing shear-thinning and shear-thickening liquids. *Journal of Non-Newtonian Fluid Mechanics*, **268**, 46–55. https://doi.org/10.1016/j.jnnfm.2019.04.001

Yin, X., & Kumar, S. (2006). Flow visualization of the liquid emptying process in scaled-up gravure grooves and cells. *Chemical Engineering Science*, **61**, 1146–1156. https://doi.org/10.1016/j.ces.2005.07.039

Received: April 27, 2025. **Revised:** September 22, 2025. **Accepted:** September 23, 2025